RSC Applied Interfaces

Accepted Manuscript

This article can be cited before page numbers have been issued, to do this please use: I. Jiménez-Morales, J. Roziere, D. J. Jones and S. Cavaliere, *RSC Appl. Interfaces*, 2025, DOI: 10.1039/D5LF00008D.

ROYAL SOCIETY OF CHEMISTRY

rsc.li/RSCApplInter

View Article Online
DOI: 10.1039/D5LF00008D

ARTICLE

A comprehensive activity-stability correlation study of tantalum-doped tin oxide as support for iridium oxide in low loading water electrolysis cell anodes

Received 00th January 20xx,
Accepted 00th January 20xx

DOI: 10.1039/x0xx00000x

Ignacio Jiménez-Morales,*[a, §] Jacques Rozière,[a] Deborah Jones,[a] Sara Cavaliere*[a]

The systematic study of the impact of the treatment temperature of IrO_x supported onto doped-tin oxide (1 at.% Ta-SnO_2 and 10 at.% Sb-SnO_2) fibres led to electrocatalysts with high activity toward oxygen evolution reaction and high resistance to degradation, allowing to comparable electrolysis performance to unsupported commercial IrO_2 with seven times higher loading.

1. Introduction

Sustainable and clean energy sources are needed to avoid the use of fossil fuels and limit environment pollution and global warming[1]. Among them, solar and wind renewable energy sources suffer from intermittency and uneven distribution, which need the development of efficient energy storage and conversion technologies. Hydrogen is a clean energy carrier enabling the storage of electrical energy with high specific weight energy density and its further conversion *via* fuel cells occurs with no carbon emissions. Green hydrogen can be produced by proton exchange membrane water electrolysis (PEMWE) coupled with renewable sources, which leads to high purity, efficiency, production rate, safety as well as rapid control response capabilities[2,3]. PEMWE can also operate at high current densities even at moderate temperatures reducing the operational costs, and the polymer electrolyte membrane used generally has low gas crossover, allowing operation under a wide range of power inputs. In addition, this process uses smaller mass-volume characteristics, no corrosive electrolyte is involved and low maintenance is needed[2–4]. In contrast, one of the foremost issues in PEMWE is the scarcity and high cost of the constituting electrode materials, in particular unsupported platinum group metals (PGMs) and/or oxides of iridium or ruthenium with a high loading, due to the low catalyst utilisation, to electrocatalyse the anodic oxygen evolution reaction (OER)[5]. IrO_2 is the most used OER catalyst due to its high corrosion resistance, and it shows only slightly lower activity than RuO_2, which is less stable at high cell voltages[5,6]. The use of binary IrO_2-RuO_2 solid solutions can partially mitigate the instability of RuO[7–9]. Their activity can be enhanced by producing nanostructured or alloyed metal oxides employing different synthetic routes[10–14]. A promising approach to reduce the PGM loading at the anode is the utilisation of support materials to uniformly disperse the electrocatalyst and increase its efficiency[15–18]. Furthermore, the support can promote activity and stability, providing corrosion resistance in the harsh PEMWE conditions. For this reason, mainly metal oxides such as TiO_2, Ta_2O_5[19,20] and SnO_2 are used[21–25], which can also interact by electron transfer with the electrocatalyst, affecting its activity. Catalyst-support interactions[26–30] modify the catalyst activity through modification of the electron density around the active sites, as identified by XPS, XRD or XAS analyses. Tin oxide has been extensively used as electrocatalyst support for ORR and OER catalysts due to its high resistance to corrosion. To enhance its intrinsically low electrical conductivity, aliovalent ions such as niobium, antimony and tantalum ions were introduced in its structure in atomic percent (n doping)[24,28,31–36]. Depending on the synthetic route as well as the doping agent used, its chemical structure, size, morphology and textural properties can be tuned.

To enhance the electrochemical stability while keeping the OER activity, the crystallinity of the IrO_2 electrocatalyst plays a crucial role. Its degree of crystallinity can be modified by thermal treatments[37–40]. Thermally treated supported IrO_2 nanoparticles demonstrated high mass activity retention after potentiostatic stability test[41]. However, a decrease of the OER activity is expected due to the drop in intrinsic OER activity for Ir (IV) species formed upon thermal treatment over Ir(III) species[12,42]. A trade-off needs to be found for iridium oxide, allowing sufficient crystallinity and stabilisation and electroactivity.

This work aims at tackling the main challenge of PEMWE anodes of keeping high activity and stability with minimum PGM loading, and reports a low-loaded anode of homogenously dispersed IrO_2 nanoparticles supported on doped tin oxide nanofibres. Antimony and tantalum doped tin oxide (ATO and TTO) fibres have already demonstrated as promising supports for electrodes experiencing high potentials (anodes in water

[a] *ICGM, University of Montpellier, CNRS, ENSCM, 34095 Montpellier Cedex 5, France.*
[§] *Current address: Department of Inorganic Chemistry, University of Salamanca, GIR-QUESCAT Group, Pl. Caídos, 37008 Salamanca, Spain*
**Corresponding authors:*
E-mail addresses: ijimenezm@usal.es, sara.cavaliere@umontpellier.fr
Supplementary Information available: [details of any supplementary information available should be included here]. See DOI: 10.1039/x0xx00000x

electrolysis and cathodes in fuel cell) with high resistance to corrosion combined with decent electronic conductivity (maxima for 10 at.% Sb and 1 at.% Ta) and surface area, and high electronic interaction with the catalyst[24,27,28,33]. In particular, 10 at.% ATO presented a conductivity similar to that of carbon (1 S cm^{-1}), but suffered from Sb leaching at potentials higher than 1.9 V/RHE[24]. 1 at.% TTO, with a ten-time lower conductivity, still adapted for the application and a slightly lower surface area (27 vs 35 m^2 g^{-1}) than ATO, evidenced no leaching of the doping agent up to 2.5 V[28]. The objective of this work is to compare their use as supports in OER both in RDE and single electrolysis cell and their interaction with the iridium-based catalyst as a function of the treatment temperature and the crystallisation of the latter.

The results of the physico-chemical and electrochemical characterisation in both 3-electrode configuration and PEMWE single cell are used to rationalise the enhanced electrochemical performance and resistance to degradation compared to unsupported commercial IrO_2, and the role of catalyst crystallinity and of the tin oxide support on the electrocatalytic properties is discussed.

2. Results and discussion

The tantalum and antimony doped tin oxides (TTO and ATO) prepared by single-needle electrospinning and subsequent calcination[27,28,33,34] were used as electrocatalyst supports for iridium oxide (IrO_x) nanoparticles synthesised by a microwave-assisted polyol method [24]. The corresponding TEM micrographs are depicted in Figure 1 (more micrographs and the corresponding diameter distribution histograms are displayed in Figure SI 1). Unsupported IrO_x nanoparticles were also prepared using the same procedure for comparative purposes (Figure SI 1f).

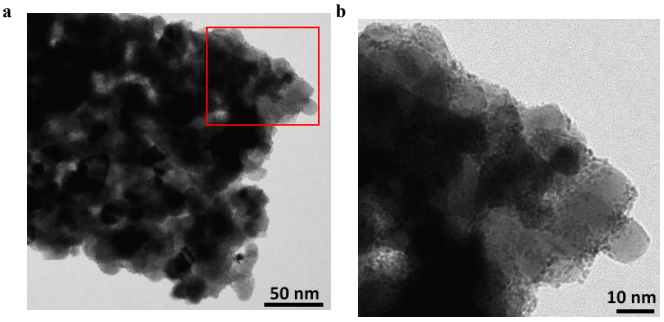

Figure 1. TEM micrographs of 16/TTO at different magnifications (b is the zoomed area in red in figure a).

IrO_x nanoparticles were deposited on TTO nanofibres at several loadings ranging from 5 to 25 wt. % (Figure SI 1) showing a progressively complete nanofibre coverage, resulting in agglomerate-free homogeneous distribution. The loading on ATO was set at 23 wt% according to a previous optimisation[28,33]. The surface saturation of TTO seemed reached at lower loading than for 23/ATO, which may be related to its lower surface area (-23 % compared to ATO) as reported elsewhere[28,33]. Comparable narrow size distributions of IrO_x nanoparticles, with an average diameter of 1.2 nm, homogeneously dispersed onto the different supports were observed in each case (Figure SI 1). The iridium loading for supported materials was determined by XRF and SEM-EDX analysis as depicted in Table 1, and in agreement with the nominal value. The O/Ir atomic ratio for unsupported IrO_x nanoparticles determined by XRF and EDX was 2.3 and 2.4 respectively, indicating a proportion of oxygen species (OH and/or H_2O groups) higher than expected from stoichiometry, which will be further discussed after TG-QMS-DSC and XPS analyses. For this reason, the as-prepared, non-thermally treated catalysts are referred as IrO_x in the manuscript.

Table 1. IrO_x content on TTO and ATO determined from XRF and SEM-EDX analyses.

Electrocatalyst	IrO_x wt.%		
	Nominal	XRF	SEM-EDX
6/TTO	5	5.7 ± 0.2	5.9 ± 0.2
12/TTO	10	11.9 ± 0.3	12.2 ± 0.4
16/TTO	15	16.1 ± 0.4	16.3 ± 0.7
19/TTO	20	19.0 ± 0.6	19.3 ± 0.9
24/TTO	25	24.2 ± 0.7	24.0 ± 0.9
23/ATO	25	22.8 ± 0.8	23.2 ± 1.0

XRD patterns analysis of all the catalysed materials as well as on pristine doped-tin oxide supports and unsupported IrO_x nanoparticles are displayed in Figure 2. IrO_x nanoparticles appear amorphous, and after their deposition on both electrocatalyst supports, only diffraction peaks corresponding to SnO_2 rutile structure (JCPDS 41-1445) are observed, while no diffraction peaks corresponding to iridium oxide were detected. Similar results have been previously reported[11,35,43], indicating that the catalyst phase is formed by amorphous clusters of hydrated IrO_x and/or consists of very small crystals lacking sufficient long-range ordering to be detected by XRD, which is in agreement with the average nanoparticles size obtained by TEM analysis (*ca.* 1.2 nm). As the amount of amorphous IrO_x deposited increased on SnO_2, the intensity of the peaks of the latter decreased (Figures 2 and SI 2).

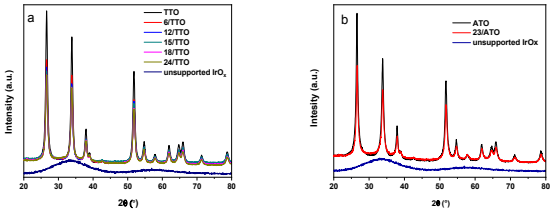

Figure 2. XRD diffraction patterns for doped tin oxide supports and with different IrO_x loadings (6-24 for TTO (a) and 23 wt.% ATO (b), respectively) as well as unsupported IrO_x.

After the synthesis, thermal treatments in the range 300-550 °C were carried out on the prepared electrocatalysts to increase the crystallinity of iridium oxide and assess the evolution of its OER activity and resistance to degradation.

Thermogravimetry quadrupole mass spectrometry differential scanning calorimetry (TG-QMS-DSC), X-ray thermodiffractometry (TDX) and TEM analysis were carried out on supported and unsupported IrO_x nanoparticles (16/TTO, 24/TTO and 23/ATO) to investigate the effect of post-synthesis thermal treatments on the thermal stability, crystallinity and size of the nanocatalysts.

The results obtained by TG-QMS-DSC are reproduced in Figure SI 3. In the TG curve of unsupported IrO_x nanoparticles (Figure SI 3b), a continuous weight loss is observed related to initial H_2O loss (5.6 wt.%) up to 193 °C, and a weight loss of 11.4 wt.% up to 600 °C, which is attributed to decomposition of OH groups present on the IrO_x surface. In agreement with this conclusion, mass spectrometry analysis was carried out simultaneously with TG-DSC analysis (Figure SI 3a), revealing a constant removal of water and OH groups (m = 17 and 18 a.u.)[44], the corresponding signals reaching their maximum at

185 and 300 °C. These results are consistent with DSC curves displayed in Figure SI 3b indicating three exothermic peaks, at 193, 297 and 460 °C assigned to the removal of physisorbed water, crystallisation of IrO_x nanoparticles [44,45] and oxidation of Ir(III) to Ir(IV)[46]. This might suggest that unsupported IrO_x nanoparticles prepared by microwave-assisted polyol method exhibit an elevated percentage of hydroxyl groups and can, therefore, be considered as an Ir-oxyhydroxide, $IrO_x(OH)_y$. This could explain the high amount of oxygen detected by XRF in comparison with the expected IrO_2. It has been reported that hydrous IrO_x, highly covered by electrophilic oxygen ligands, covalently linked to the metal, possess high OER catalytic activity[47,48].

Comparable TG curves (Figure SI 3c and 3d) were obtained for the catalysed materials although they exhibited lower mass losses, despite performing the analysis with similar IrO_x mass as with unsupported material. This may be attributed to the high dispersion and improved interaction of IrO_x nanoparticles on the oxide supports. Higher mass loss was observed for the catalyst supported on ATO than on TTO, in agreement with its higher catalyst loading. From the DSC curves of the catalysed materials only two exothermic peaks were observed, the former at slightly lower temperature (180 °C) than for unsupported IrO_x, and the latter around 297-310 °C, attributed to the phase transition from amorphous to crystalline iridium oxide, referred as IrO_2.

The crystallisation of IrO_x to IrO_2 with temperature was monitored by X-ray thermodiffractometry (Figure 3). Peaks of the rutile structure of IrO_2 appeared by increasing the treatment temperature confirming the presence of crystalline particles. The analysis of supported and unsupported IrO_x nanoparticles demonstrated that at temperatures lower than 300 °C, no new diffraction peaks were observed unless those corresponding to SnO_2 rutile structure.

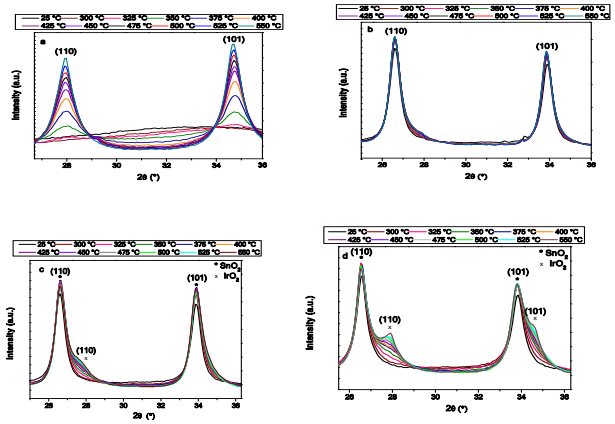

Figure 3. X-ray thermodiffraction patterns of a) unsupported IrO_x nanoparticles, b) 16/TTO, c) 24/TTO and d) 23/ATO.

Starting at 300 °C diffraction peaks at 28 ° and 34.7 ° appeared corresponding to iridium oxide (JCPDS 15-0870). Such peaks became progressively more defined as the treatment temperature increased, which may be related to the progressive crystallisation of IrO_x nanoparticles, as well as to their coalescence and growth. It is interesting to notice the effect of the support on the crystallisation and growth of IrO_2 particles. It may be observed from Figure 3c and 3d that a reduced IrO_2 peak formation is detected for TTO compared to ATO: in the same conditions of catalyst loading and treatment temperature, the crystallisation of IrO_x is favoured on ATO suggesting a different catalyst/support interaction. The average crystallite size achieved at 350 °C (when IrO_2 peaks are more prominent, allowing peak deconvolution) were 5.8 and 4.2 nm (Scherrer equation applied to the (110) peak) for unsupported and supported (24/TTO and 23/ATO) IrO_2, respectively. At lower loading (16 wt.%) the diffraction peaks of iridium oxide in TTO-supported IrO_2 in XRD due to the low size and high dispersion of the nanoparticles. In order to assess top surface crystallisation, Raman spectroscopy was performed. Comparison of the Raman spectra of 16/TTO/300 and TTO reveals the appearance of two lines at 542 and 713 cm^{-1} (Figure SI 6), confirming the presence of crystallised iridium oxide at the support surface. The former line corresponds to the E_g mode, while the latter is attributed to the overlapping vibrational modes B_{2g} and A_{1g}. Regarding major vibration modes E_g and B_{2g} for IrO_2 at 561 and 728 cm^{-1},[49–51] these bands are red-shifted and assigned to the Ir–O stretching vibrations coupled with O–H bending vibrations in the Ir–(OH) structure[51,52], in agreement with the coexistence of amorphous–crystalline IrO_2. All these results are in agreement with the DSC analysis and lead us to conclude that a post-synthesis treatment at temperature around 300 °C is needed for the transition from amorphous to crystalline structure to occur, which has been already demonstrated to be more stable to degradation[53–55]. However, a loss of electrochemical activity is expected due to the reduced amount of Ir(III) and iridium hydroxide groups[55–57].

The evolution of supported and unsupported IrO_x nanoparticles upon thermal treatment was also monitored by TEM and electron diffraction analyses (Figure SI 4 and 5). Whereas as-synthesised unsupported IrO_x nanoparticles exhibited no diffraction pattern (Figure 4b), after treatment at 300 °C the SAED displayed an initial transition to a crystalline material, which was finalised at 325 ° C (Figure SI 4d and 4f) in agreement with thermal and structural analysis results. In the absence of support, no isolated nanoparticles were detected by HRTEM, but instead a self-organised array (Figure SI 4a), which might be related to nanoparticle self-interactions. Such particles sinter and increase in size after the thermal treatment reaching, at 300 °C, an initial coalescence with an average nanoparticle size of 2.4 nm (Figure SI 4c), which increased at 325 °C leading to the formation of agglomerates (Figure SI 4e).

Significant changes in size and distribution of supported iridium oxide nanoparticles after treatment at 300 °C were detected by TEM (Figure SI 5). The nanoparticles supported on ATO nanofibres (Figure SI 5a, b) exhibited an increase in size to *ca.* 2.0 nm. The lower average nanoparticle size reached compared to unsupported catalysts suggests that their interaction with the support stabilise their growth, avoiding agglomeration and favouring homogeneous dispersion. 16 wt.% IrO_x loaded TTO treated at 300 °C exhibited homogeneous nanocatalyst dispersion (Figure SI 5c), while at higher loadings, for instance 24/TTO/300, only IrO_2 nanoparticles agglomerates were observed (Figure SI 5e). This might indicate that nanofibre over-coverage was reached. For the same catalyst loading, the ATO based catalyst did not present over-coverage, which may be related to the slightly higher developed surface area of this support. These results suggest that a low catalyst loading is desired to achieve high dispersion without agglomeration on tantalum doped SnO_2 fibres. The optimal IrO_2 loading on the TTO nanofibres support that was further investigated by electrochemical methods was therefore 16 wt.% (sample 16/TTO).

X-ray photoelectron spectroscopy (XPS) was carried out to investigate the surface chemical state of unsupported IrO_x nanoparticles and of IrO_x/TTO with several catalyst loadings ≥ 16 wt.%, in comparison with 23/ATO and the bare support (Figure 4). High resolution spectra were recorded for Ir, O and Sn. Owing to the small size of the IrO_x particles, it was assumed that both bulk and surface species contribute to the XPS signals. Ir 4f core level spectra

for all catalysed materials and unsupported IrO_x nanoparticles presented the conventional asymmetrical shape[58], indicating two oxidation states related to Ir(IV) (A and A' corresponding to $Ir4f_{7/2}$ (61.9 eV), and $Ir4f_{7/2}$ satellite (63.1 eV), respectively) and Ir(III) (B and B' corresponding to $Ir4f_{7/2}$ (62.4 eV), $Ir4f_{7/2}$ satellite (63.5 eV), respectively) (Figure 4a)[10,30,44,59]. Ir (III)/ Ir(III) + Ir(IV) proportion of 26.7 % was found for the IrO_x particles synthesised by microwave-assisted polyol method, in agreement with the amorphous nature of the catalyst [60]. The XPS core level spectra of Ir 4f for all supported-IrO_x electrocatalysts, shown in Figure 4b, exhibit a negative shift compared to unsupported IrO_x nanoparticles (62.1 eV), suggesting an increase of highly oxidised iridium. This is in contrast to previous observations of lower average Ir and Pt oxidation state in the oxide-supported IrO_x nanoparticles compared to the carbon-supported ones [27,30]. This peak shift is more evident for lower catalyst loadings onto TTO (exacerbating IrO_x/TTO interactions *vs* IrO_x /IrO_x interactions). The XPS high-resolution spectra of the O1s and Sn3d regions for bare and catalysed TTO are reported in Figure 4c and 4d, respectively. Core level spectra of Sn3d show a doublet at 486.9 and 495.3 eV, attributed to Sn (IV) considering the peak position and the their gap, although keeping in mind that Sn (II) may also be present but being difficult to analyse by XPS[61,62]. For O1s core level spectra, a broad peak ranging from 528 to 535 eV can be deconvoluted in two contributions. The one at lower binding energy (band A') assigned to O^{2-} in an oxide lattice structure and that at higher binding energy (band B') to H_2O, OH or CO species adsorbed on the surface, in agreement with the presence of hydrous IrO_x phase. No third contribution at 533 eV (band C) was detected for catalysed materials in comparison to unsupported IrO_x nanoparticles due to higher proportion of electrocatalyst support. As for Ir 4f peaks, a shift of Sn 3d and O1s peaks is observed compared to bare supports. These results suggest an electronic coupling effect corresponding to interfacial electron transfer between the support and the iridium oxyhydroxide centres of the catalyst nanoparticles[27,28,30,63,64]. The results displayed in Figure 4b demonstrate that at the lower the IrO_x loading on TTO, the higher was the downshift of the Ir 4f bands, suggesting a stronger interaction and charge transfer with the support. For 16/TTO the shift was of 0.3 eV. For 24 % IrO_x loading, this effect disappeared and almost the same binding energy of unsupported nanoparticles was observed, suggesting that nanofiber over-coverage leads to prevailing interparticle interaction over nanoparticle/support ones. After thermal treatment, 16/TTO/300 exhibited a lower shift to higher binding energy (0.1 eV), which suggests a reduced electronic coupling effect compared to the as-synthesised material. For IrO_x deposited onto ATO a slight shift of the Ir 4f peak compared to TTO was observed (61.8 eV). The shift in binding energy for Sn3d and O1s core level spectra compared to the bare support (Figure 4c and 4d), also depends on the amount of catalyst deposited on TTO. It is interesting to notice that the shift is positive for the catalysed ATO, and negative in the case of TTO. As already observed for the IrO_x crystallisation (TDX analysis), this result demonstrates the role of the nature of the doping agent of the support on the interaction with the electrocatalyst and its overall properties. The sample 16/TTO treated at 300 °C showed a lower downshift in the Sn3d and O1s core level spectra compared to the non-treated one (0.2 eV and 0.3 eV, respectively) suggesting lower interaction and lower proportion of the hydrous IrO_x phase, in agreement with XRD and TG-QMS-DSC analysis.

The OER activity of the catalysed supports before and after the thermal treatment at 300 °C was determined in N_2-saturated 0.5 M H_2SO_4 at 20 °C using a rotating speed of 1600 rpm. OER polarisation curves normalised to iridium mass are reproduced in Figure 5 after iR correction and the extracted electroactivity data listed in Table 2. OER polarisation curves normalised to the geometric disk area before and after iR correction are presented for comparison in Figure SI 7a and 7b. The corresponding Tafel plots are presented in Figure SI 8. As prepared 16/TTO and 23/ATO exhibited the highest OER activities (137 and 144 A g_{Ir}^{-1} at 1.5 V/RHE, respectively). Despite the lower electrical conductivity of TTO and the lower IrO_x loading on this support, the electrocatalytic activity of 16/TTO is the same of 23/ATO, which may be ascribed to the synergy between the catalyst and the support (similar XPS peak shifts observed for those samples). Samples with IrO_x loading lower than 16 wt.% show a reduced OER activity, probably due to a more pronounced resistive effect of the support. On the other hand, at IrO_x loading higher than 16 wt.% on TTO, lower performance was observed, which can be ascribed to the overcoverage of the support, leading to reduced catalyst-support interaction effect as observed by XPS[57]. The analysis of the electrochemical surface area(ECSA) of the catalysed materials was performed[58] (Table SI 1). The results indicate higher ECSA values for 16/TTO and 23/ATO, which confirm the enhanced catalyst utilisation and align with the higher electrocatalytic activity observed for these electrocatalysts.

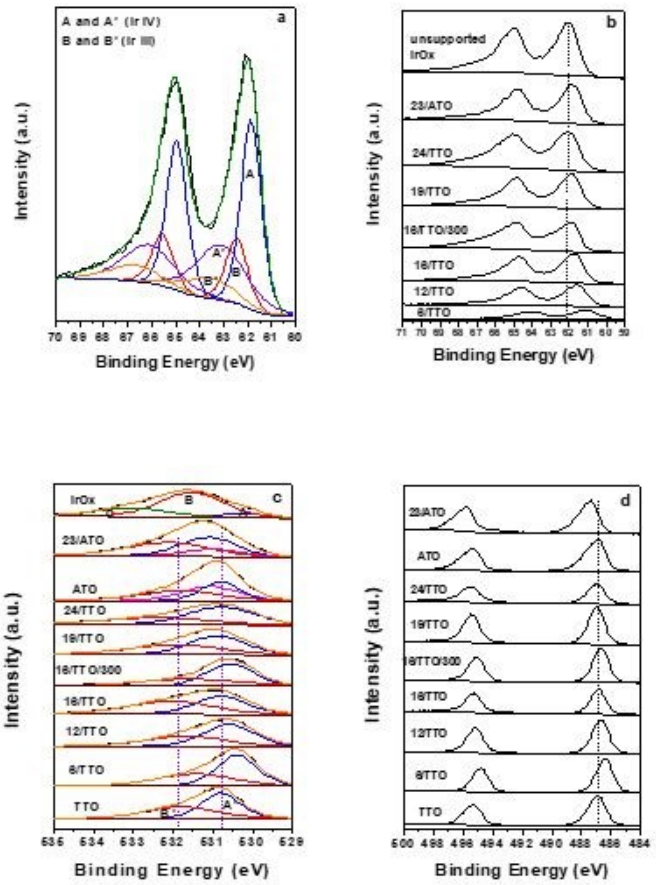

Figure 4. XPS core level spectra of Ir 4f for unsupported IrO_x nanoparticles deconvoluted (a), XPS core level spectra of Ir 4f (b), O1s (c) and Sn 3d (d) for catalysed materials also after thermal treatment in comparison with unsupported IrO_x and bare supports.

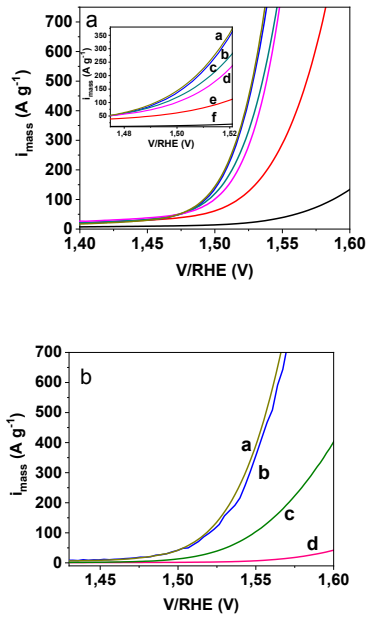

Figure 5. OER polarisation curves Ir-normalised mass current density for a) non-treated (with an enlarged graphic in insert) and b) thermally treated electrocatalysts: a) 23/ATO/300, b) 16/TTO/300, c) 19/TTO/300, d) 24/TTO/300, e) 12/TTO and f) 6/TTO.

Table 2. Catalytic performance for pristine and thermally treated catalysed supports.

Electrocatalyst	Mass activity (A g^{-1}) at 1.5 V/RHE	Overpotential (mV) at 10 mA cm^{-2}
6/TTO	14±4	449
12/TTO	62±7	342
16/TTO(300)	137±11 (48±8)	302 (332)
19/TTO(300)	122±9 (14±4)	309 (389)
24/TTO(300)	103±8 (2±1)	314 (505)
23/ATO(300)	144±13 (51±10)	301 (326)

Electrochemical characterisation was also performed on the electrocatalysts treated at 300 °C presenting therefore the beginning of crystallisation of the iridium oxide phase. As expected, the activity dropped and the overpotential increased. 16/TTO/300 demonstrated the highest OER activity (48 A g^{-1} at 1.5 V) among the treated IrO_2/TTO (Table 2). Increasing the catalyst loading, the electroactivity dropped until 2 A g^{-1} at 1.5 V for 24/TTO/300, demonstrating the effect of overcoverage combined with particle growth and aggregation due to the thermal treatment. Thermally treated 23/ATO/300 presented similar activity (51 A g_{Ir}^{-1} at 1.5 V) than 16/TTO/300.

To further optimise the electrocatalyst presenting the highest activity, 16/TTO, and verify the choice of the thermal treatment at 300 °C, its electrochemical activity and stability was assessed after thermal treatments between 200 and 325 °C. OER polarisation curves normalised to the geometric disk area before and after iR correction are displayed in Figure SI 7c. The electrochemical degradation of the different treated TTO based catalyst was monitored by evaluating the OER activity before and after performing chronoamperometry measurements at a current density of 10 mA cm^{-2} for 20 h (Figure 6). As expected, an increase in treatment temperature led to a reduced OER activity, while enhancing the resistance to degradation. All Tafel slopes increased under similar accelerated stress test conditions, indicating electrocatalyst degradation ascribed to increased nanoparticle sizes and/or Ir-dissolution[40,65]. This study highlighted that the 16/TTO catalyst treated at 300 °C gave rise to the best activity-stability trade-off (Figure 6c).

These results are in agreement with a) those obtained by TG-QMS and XPS indicating that the decrease in the activity is related to the loss of OH groups and b) those of TG-DSC, TDX and HRTEM confirming the formation of the IrO_2 crystalline phase at 300 °C with homogeneous distribution. Despite the similarity highlighted by the range of characterisation techniques for 16/TTO/300 and 23/ATO/300 (Figure 6b), the latter displays a lower resistance to degradation, which could be related to instability of antimony as dopant as reported elsewhere[24,66]. These results shed light on the double role of tantalum doping agent on the catalysed material activity (48 ± 8 A g^{-1} at 1.5 V/RHE) and the electrocatalyst support stability after 20 h (32 ± 4 A g^{-1} at 1.5 V) keeping a mass activity retention of 65 % and a slight increase on the overpotential of 22 mV. Overall, 16/TTO/300 demonstrated higher OER activity and stability compared to similar supported catalysts[16,36,41,67–69].

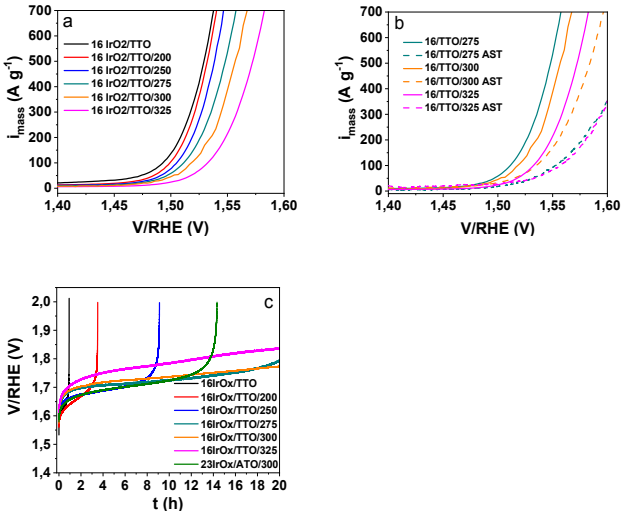

Figure 6. Ir-mass normalised OER polarisation curves obtained with the catalysts indicated in the legend before (a) and after (b) chronopotentiometry measurements at 10 mA cm^{-2} for 20 h (c).

Finally, the electrocatalyst 16/TTO treated at different temperatures around 300 °C was characterised at the anode side of a water electrolysis cell, in order to find the best compromise between performance and durability in MEA operating conditions. The charge of the anode was kept ultra-low (< 0.2 mg_{Ir} cm^{-2}) and the MEA results were compared with those obtained with commercial benchmark with conventional high charges.

The MEAs investigated included 0.18 mg_{Ir} cm^{-2} anodes based on 16/TTO treated at 275-300-325 °C, a Nafion 115 membrane and a 0.5 mg_{Pt} cm^{-2} Pt/C commercial GDE cathode. Their corresponding polarisation curves in electrolysis cell as well as electrochemical impedance spectra at 80 °C and a range of current densities are displayed in Figure 7 and SI 9 as well as in Table 3 and Table SI 2. As it can be observed from i/V curves, and in agreement with the *ex situ* electrochemical measurements, the average voltage at 1.0 and 1.5 A cm^{-2} increased with the treatment temperature of the anode catalyst. EIS analysis showed an almost identical ohmic resistance for all the MEAs, and enhanced charge transfer resistance as the treatment temperature of the supported anode catalyst increased. This is in agreement with a lower electrocatalytic activity and results reported in literature[70]. To assess the effect of electrocatalyst

thermal treatment on its stability, the i/V curves were recorded before and after an accelerated stress test consisting in polarising the cell at 2.0 V (Figure 7a and Tables 4 and SI 1).

It is evident that all MEAs lost performance after the polarisation at high potential. The drop was higher for the MEA including the anode electrocatalyst treated at 275 °C (1.89 V at 1 A cm^{-2}) and lower for that with the anode electrocatalyst treated at 300 °C (1.77 V at 1 A cm^{-2}), as expected with the increasing degree of crystallisation assessed by TDX and TG-DSC analysis. However, for the MEA comprising the most crystalline electrocatalyst, 16/TTO/325 °C, the stability was lower (1.85 V at 1 A cm^{-2}), probably due to the agglomeration state of the catalyst induced by the higher treatment temperature. Such results were further interpreted after carrying out end of test (EoT) analysis on the different MEAs by SEM-EDX and ICP-MS of anode exhaust water (Table SI 3 and Figure SI 10). The latter indicated no significant leaching of elements from the oxide support either from the electrocatalysts treated at 300 and 325 °C. TEM and EDX analysis of both MEAs after test (Figure SI 11 and Table SI 3) demonstrate that iridium oxide particles coalescence was more prominent for the sample treated at 325 °C in agreement with its higher performance drop.

In conclusion, MEA characterisation confirmed that 16/TTO/300 presents the best trade-off between OER activity and stability. A further comparison was made with an MEA with antimony doped-tin oxide as OER electrocatalyst support. Figure 7c and Tables 4 and SI 1 present the comparison of results between MEAs with a charge of 0.18 mg_{Ir} cm^{-2} at the anode side based on 23 wt.% IrO_2/ATO and 16 wt.% IrO_2/TTO treated at 300 °C. It can be observed a slight improvement in the performance and ohmic and charge transfer resistance in the activation region for the 23/ATO/300, which might be attributed to the 10-time higher electrical conductivity of the support, while similar resistance is observed for the ohmic and mass transport region (the used membrane was the same). However, greater performance loss and ohmic and charge transfer resistances were evident after the degradation protocol up to 2.0 V. This result was ascribed to the instability of antimony in SnO_2 detected by EDX and ICP-MS analysis (Table SI 3 and Figure SI 10) and reported elsewhere[24,66], possibly leading to a drop in conductivity of the support material and therefore to nanocatalyst deactivation.

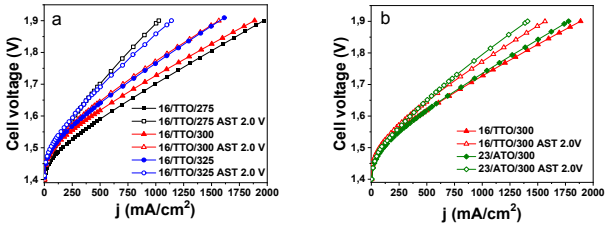

Figure 7. I/V curves at 80 °C for MEAs based on a) 16/TTO treated at the different indicated temperatures at the anode side before and after the stability test at 2.0 V, b) 16/TTO/300 and 23/ATO/300 at the anode side before and after stability test at 2.0 V.

Table 3. Catalytic performance of electrocatalysts thermally treated before (and after) stability test in an electrolysis cell at 80 °C.

OER catalyst	Cell voltage (V)		Mass activity (A g_{Ir}^{-1})	Tafel slope (mV dec^{-1})	Overpotential at 10 mA cm^{-2} (mV)
	@ 1 A cm^{-2}	@ 1.5 A cm^{-2}	@ 1.5 V		
16/TTO/275	1.70 (1.89)	1.81 (>2)	901 (508)	61 (72)	184 (188)
16/TTO/300	1.73 (1.78)	1.83 (1.89)	498 (429)	56 (58)	210 (213)
16/TTO/325	1.76 (1.86)	1.88 (>2)	408 (310)	59 (66)	214 (217)
23/ATO/300	1.74 (1.80)	1.84 (1.92)	617 (490)	60 (64)	200 (202)

In general, similar performance are reported for MEAs including Ir-based catalysts supported on other types of metal oxide, but using higher noble metal loading at the anode than in this work (0.18 mg_{Ir} cm^2 of 16/TTO/300)[15,68,69,71–74].

The promising results for 16/TTO/300 as PEMWE anode with a low loading (0.18 mg_{Ir} cm^{-2}) confirm that despite the lower conductivity and relatively low surface area of the tantalum doped tin oxide nanofibrous support, the catalysed material exhibits a high activity (498 A g_{Ir}^{-1} at 1.5 V) and a remarkable resistance to corrosion (83 % of mass activity retention after AST at 1 A cm^{-2}), which can be rationalised by the strong metal oxide-support interaction and the stability of TTO. To conclude this study a comparison of MEAs bearing such anode catalyst with low iridium loading (0.18 mg cm^{-2}) was performed with an otherwise identical MEAs based on commercial unsupported IrO_2 catalyst with conventional 7 times higher PGM loading (1.28 mg cm^{-2}), highlighting similar performance (Figure 8).

In conclusion, the 16 wt.% IrO_x/TTO catalyst treated at 300 °C demonstrated a high stability and activity in RDE as well as in PEMWE single cell, reaching the performance of an MEA including an unsupported commercial OER catalyst with 7 time more iridium, with great perspectives towards the reduction of this PGM metal for decarbonated hydrogen production.

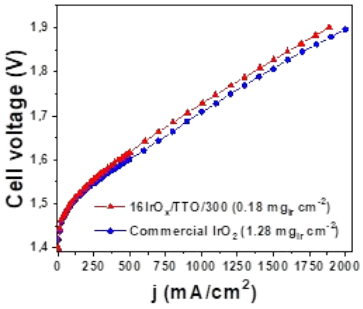

Figure 8. Polarisation curves of MEAs including 16/TTO/300 or commercial IrO_2 with 7 times higher Ir loading at the anode.

3. Experimental

3.1 Preparation of TTO and ATO nanofibres

1 at.% tantalum doped SnO_2 fibres (TTO) and 10 at.% antimony doped SnO_2 fibres (ATO) were prepared by electrospinning and thermally treated according to a previously reported synthesis[27,28,33,34].

3.2 Preparation of IrO_x supported onto TTO and ATO

A microwave-assisted polyol method was used to prepare nanoparticles of iridium oxide [24,75]. In a typical experiment, a 0.78 g L^{-1} solution of hydrogen hexachloroiridate(IV) hydrate ($H_2IrCl_6 \cdot xH_2O$, Sigma Aldrich 99.98%) in nitrogen-saturated ethylene glycol (40 mL, Sigma Aldrich 99.8 %) was prepared, and its pH adjusted to 11 with NaOH (1 M solution, Sigma Aldrich 98 %). The solution was transferred to a microwave reactor (MiniFlow 200XX Sairem) and the reaction carried out at 180 °C for 20 minutes at 160 W under oxygen atmosphere. The resulting IrO_x nanoparticle suspension was cooled down to room temperature, and then sonicated for 20 min (Branson Digital Sonifier®) after addition of the corresponding TTO or ATO doped-SnO_2 support materials to reach the targeted loading. Afterwards, the suspension was diluted by the addition of 50 mL of water, and the pH adjusted to 1 by adding HNO_3 (65 %, Sigma

Aldrich). After five minutes at constant pH, the IrO_x/doped-SnO_2 materials were recovered by filtration, washed with Milli-Q® grade water, and dried at 80 °C for 24 h. The samples were labelled x/TTO and x/ATO where x indicates the targeted catalyst loading on TTO and ATO, namely 5, 10, 15, 20 and 25 wt.% IrO_x on TTO nanofibres and 25 wt.% IrO_x on ATO nanofibres since, as we previously reported[24], this loading provides the highest performance.

Further thermal treatment of the supported IrO_x materials using a ramp rate of 5 °C min^{-1} for 2 h at temperatures ranging from 300 °C to 550 °C was carried out to study its effect on catalyst nanoparticle size and crystallinity degree, and the resulting impact on the electrochemical activity and stability of the supported catalysts. Thermally treated samples were labelled x/TTO/y and x/ATO/y, where y indicates the temperature of applied thermal treatment.

3.3 Physicochemical characterisation of IrO_x/TTO

The morphology of IrO_x/TTO was analysed using a scanning electron microscope (SEM) FEI Quanta FEG 200 equipped with energy-dispersive X-ray spectroscopy (EDS) analysis, and using a JEOL 1200 EXII transmission electron microscope (TEM) operating at 120 kV, equipped with a SIS Olympus Quemesa CCD camera (11 million pixels). For TEM analysis the samples were suspended and sonicated in ethanol, then deposited onto carbon-coated copper grids, while for cross-sectional analysis in SEM, a microtome was used to cut resin-encapsulated electrocatalyst powders and the corresponding slices were deposited onto copper grids. The average size of iridium oxide particles and tin oxide fibres was determined by measuring 200 selected objects using the ImageJ software. A FEI Talos F200X microscope operated at 200 kV (Schottky-FEG emitter) and fitted with an in-column omega-filter and a GATAN Ultrascan CCD 2048 × 2048 px2 camera was used to obtain high-resolution TEM (HRTEM) micrographs and the corresponding selected area electron diffraction (SAED) (0.23 nm point resolution).

Powder X-ray diffraction (XRD) patterns were recorded at 20 °C in Bragg-Brentano configuration using a PANalytical X'pert diffractometer, equipped with a hybrid monochromator, operating with CuK_α radiation (λ = 1.541 Å). A step size of 0.1° 2θ within the 2θ domain from 20° to 80° was employed.

X-ray thermodiffractometry (TDX) was performed to study crystal structure changes and its characterisation were monitored by an *in situ* high temperature XRD using a Malvern-Panalytical Empyrean diffractometer series 2, equipped with an Anton-Paar HTK 16 high-temperature camera (CoK_α - radiation). For each sample, employing a step size of 0.1° and 2θ range from 25° to 36°, a sequence of XRD measurements was performed at room temperature and again after each heating step of 25 °C (ramp rate of 5 °C/min) in the temperature range from 300 °C to 550 °C, with the sample cell under vacuum of 10^{-3} Torr, and a recording time of 2 h for every diffractogram. After recording the XRD pattern at 550 °C, the samples were cooled to 25 °C (5 °C/min) under vacuum.

X-ray fluorescence (XRF) was used to determine the iridium loading onto the metal oxide supports. Samples were prepared by grinding 50 mg of IrO_x/doped-SnO_2 with 25 mg of cellulose to form a powder that was placed in a cavity in a boric acid matrix and subsequently pressed to obtain a pellet of 32 mm diameter with scanned surface of *ca*. 12 mm. The same protocol was used to prepare six standards using 5, 10, 15, 20, 25 and 30 wt.% of IrO_2 (Sigma Aldrich, 99.9 %) and doped-SnO_2 to obtain a calibration line. The XRF analyses were performed with a PANalytical Axios Max spectrometer fitted with a Rh (4 kW) tube, and equipped with a LiF200 crystal and Omnian software.

Thermogravimetry/Differential Scanning Calorimetry coupled with Mass Spectrometry (TG/DSC/MS) analysis was carried out using a simultaneous thermal analyser model STA449F1 Jupiter® (Netzsch) (TGA/DSC) coupled to a Aeolos Quadro QMS 403 mass spectrometer in the temperature range from 25 °C to 600 °C with a heating rate of 5 °C min^{-1} under air.

Raman analysis was performed on a Renishaw inVia spectrometer with a wavelength of 532 nm, a power of 200 µW and a resolution of 1 cm^{-1}.

The surface chemical state of the materials was investigated by X-ray Photoelectron Spectroscopy (XPS) on an ESCALAB 250 (Thermo Electron) spectrometer. The X-ray excitation was provided by a monochromatic Al K_α (1486.6 eV) source and the analysed surface area was 400 μm^2. A constant analyser energy mode was used for the electron detection (20 eV pass energy), which was performed perpendicularly to the sample surface. The data were analysed in the Avantage and CASA XPS software, removing the background signal using the Shirley method. The surface atomic concentrations were determined from photoelectron peak areas using the atomic sensitivity factors reported by Scofield[76]. Binding energies of all core levels are referred to the C-C bond of C 1 s at 284.8 eV.

3.4 Electrochemical characterisation of TTO and IrO_2/TTO

Electrochemical analyses were carried out at 25 °C using a Pine bipotentiostat model AFCBP1 in a conventional three-electrode cell composed of a reversible hydrogen electrode (RHE, reference electrode), a gold rotating disk electrode (RDE) (working electrode, geometric area 0.196 cm^2), and a platinum wire (counter electrode), the reference and counter electrodes were separated from the working electrode compartment by a glass frit. Prior to evaluation of the OER activity, 10 cyclic voltammograms (CVs) were recorded in the range from 0.05 to 1.4 V *vs* RHE in N_2 saturated 0.5 M H_2SO_4 at 50 mV s^{-1} and then linear sweep voltammetry (LSV) was performed between 1.2 and 1.6 V vs RHE at 10 mV s^{-1} at 25 °C using a rotation speed of 1600 rpm. All the potential values are referred to the RHE and were corrected for the ohmic drop in solution. The current densities are reported as current per gram of iridium oxide for mass activity evaluation at 1.5 V/RHE. For instance, the catalyst ink of 24/TTO was prepared by dispersing 3 mg in 297.8 µL of Milli-Q® grade water, 893.4 µL of isopropanol (Aldrich) and 17.1 µL 5 wt.% Nafion® EW1100 solution in alcohols (Aldrich) and sonicating (VWR Ultrasonic Cleaner) for 15 min. 7 µL aliquots were deposited onto the RDE surface with a micropipette and dried in air. The Ir loading on the electrode was 17.7 µg cm^{-2} for all the electrocatalysts. To estimate the electrochemically active surface area (ECSA), the double-layer capacitance (C_{dl}) was calculated using CV scans at different scan rates (10, 20, 30, 40 and 50 mV s^{-1}) in the non-Faradaic region (0.5-0.6 V_{RHE}). After plotting the average between the maximum anodic current density and the minimum cathodic current density against the scan rate, C_{dl} of every catalysed material correspond to the slope obtained. Then, C_{dl} is converted to ECSA by diving it by the specific

capacitance in acidic conditions (0.035 mF·cm^{-2})[77] and the mass loading deposited on the electrode[58].

Chronopotentiometry measurements were performed to investigate the resistance of IrO_x/TTO and IrO_x/ATO to electrochemical degradation by holding the working electrode (gold, geometric area of 0.196 cm^2) at a constant current density of 10 mA cm^{-2} for 20 h in 0.5 M H_2SO_4 at 25 °C and assessing the evolution of the potential up to a cut-off potential of 2.0 V vs RHE. LSV was performed to determine the decay of OER activity after each 20-hour potential hold.

3.5 Preparation of membrane electrode assemblies

Membrane-electrode assemblies (MEAs) of active area 6.75 cm^2 were prepared using the decal method for the anode and a commercial Pt/C cathode. For the anode 0.18 mg_{Ir} cm^{-2} were deposited from an ink composed of the catalyst (22.7 mg of 16/TTO, 15.8 mg 23/ATO and 22.2 mg commercial IrO_2 - 99.9 wt.% Surepure® Chemetals) and a mass ratio of 20 wt.% of Nafion (from a 5 wt.% Nafion EW1100 solution in alcohols) with respect to the catalysed material dispersed in isopropanol/water (3:1) (V/V) homogenised in ultrasonic bath. This ink was sprayed onto a Teflon sheet by using a Nadetech Innovations ND-SP Spray Coater placed over a heating pad at 80 °C. A Nafion 115 membrane (Ion Power) was pre-treated to re-establish the acidic sites[78], and then employed for the decal transfer of the above catalyst layer to produce a catalyst coated membrane (CCM). For this, the membrane was placed over the sprayed catalyst layer and covered with a Teflon-glass-fibre fabric, and hot-pressed using the following steps: pre-heating at 80 °C and then applying a pressure of 8.1 MPa, increasing of the temperature to 140 °C and then the pressure to 15.7 MPa for 15 min. Similar hot-pressing conditions were used for the assembly of the cathode side (0.5 mg Pt cm^{-2} supported on a Sigracet 22BB GDL from Baltic Fuel Cells) to the prepared CCM, when 90 s were needed for its complete transfer to obtain the final MEA. A similar procedure was carried out for the preparation of a reference MEA for which commercial unsupported IrO_2 (Surepure® Chemetals) was used at the anode, with a loading of 1.28 mg_{Ir} cm^{-2}.

3.6 Single-cell electrochemical characterisation of the prepared MEAs

The MEA was integrated into the cell set-up employing fluorinated ethylene propylene gaskets and reaching a final compression of 50-55 %. After flooding the anode side with deionized water (Milli-Q quality, 18 MW), a 200 mL h^{-1} flow rate of deionized water was passed through the anode chamber and the MEA was conditioned at 80 °C for 12 h at 0.2 A cm^{-2} to ensure complete membrane hydration. The characterisation of the cell was carried out at a cell temperature of 80 °C by a Bio-logic SP-150 potentiostat with a 20 A booster. Polarisation curves were recorded in the current density range from 0 to 2 A cm^{-2}. A fixed current density was maintained until a variation of the steady-state potential was lower than 1 mV min^{-1}. Thereafter, a potentiostatic accelerated stress test (AST) was performed by holding at a potential from 1.5 to 2.0 V (with 0.1 V steps) for 4 hours to evaluate the stability of the catalysed materials. A polarisation curve was recorded after every potentiostatic step. Furthermore, *ca* 1 L of exhaust water was recovered from the anode side, 20 mL of water was withdrawn, to which 100 µL of *aqua regia* was added to dissolve any solid, and analysed by ICP-MS. Electrochemical impedance spectroscopy (EIS) measurements were performed in the frequency range 30 kHz to 100 mHz at 0.025, 0.05, 0.125 and 0.2 A cm^{-2} to measure the MEA resistance before and after the AST.

4. Conclusions

This work investigated the OER electrocatalytic activity and stability trade-off of iridium oxide nanoparticles supported onto doped-SnO_2 fibres (ATO and TTO) upon thermal treatments at different temperatures. The treatment at 300 °C led to crystallised well dispersed IrO_2 particles with high OER electrochemical activity and resistance to degradation. In particular, 16 wt.% IrO_2 catalysts supported on TTO (16/TTO/300) demonstrated higher stability both in RDE and in single-cell electrolysis test, with a mass activity retention after AST of 83 % at 1 A cm^{-2}. The performance of the MEAs comprising an anode based on 16/TTO/300 overcome that of MEAs based on commercial unsupported IrO_2 but with seven times lower iridium loading (0.18 mg_{Ir} cm^2 *vs.* 1.28 mg_{Ir} cm^2). These results confirm that 16/TTO/300 is a promising anode electrocatalyst for PEMWE and that the optimisation of crystallinity of IrO_x and the use of conducting and stable supports paves the way for the design of OER catalysts with ultra-low iridium loading. Further optimisation of the support porosity and catalyst surface area and composition can further reduce this loading, while keeping high mass activity and durability tackling one of the greatest challenges for PEMWE development.

Author contributions

I. J.-M. carried out the experimental work and wrote the initial draft. D.J., J. R. and S.C. provided supervision, and revised and edited the manuscript.

Conflicts of interest

There are no conflicts to declare.

Data availability

The data supporting this article have been included as part of the Supplementary Information.

Acknowledgements

The research leading to these results has received funding from the European Research Council under the H2020 European Union's Programme/ERC-2019-POC in the frame of the HYDROGEN project (Grant Agreement n. 875573) and the French National Research Agency in the frame of the MOISE (Grant Agreement n. ANR-17-CE05-0033) and MATHYLDE projects (Grant Agreement n. ANR-22-PEHY-0001).

References

1 S. E. Hosseini and M. A. Wahid, *Renew. Sustain. Energy Rev.*, 2016, **57**, 850–866.

2 Q. Feng, X. Z. Yuan, G. Liu, B. Wei, Z. Zhang, H. Li and H. Wang, *J. Power Sources*, 2017, **366**, 33–55.
3 S. A. Grigoriev, V. N. Fateev, D. G. Bessarabov and P. Millet, *Int. J. Hydrogen Energy*, 2020, **45**, 26036–26058.
4 P. Millet, N. Mbemba, S. A. Grigoriev, V. N. Fateev, A. Aukauloo and C. Etiévant, *Int. J. Hydrogen Energy*, 2011, **36**, 4134–4142.
5 A. Marshall, B. Børresen, G. Hagen, M. Tsypkin and R. Tunold, *Energy*, 2007, **32**, 431–436.
6 O. Kasian, S. Geiger, P. Stock, G. Polymeros, B. Breitbach, A. Savan, A. Ludwig, S. Cherevko and K. J. J. Mayrhofer, *J. Electrochem. Soc.*, 2016, **163**, F3099–F3104.
7 T. Audichon, E. Mayousse, S. Morisset, C. Morais, C. Comminges, T. W. Napporn and K. B. Kokoh, *Int. J. Hydrogen Energy*, 2014, **39**, 18785–16796.
8 T. Audichon, T. W. Napporn, C. Canaff, C. Morais, C. Comminges and K. B. Kokoh, *J. Phys. Chem. C*, 2016, **120**, 2562–2573.
9 S. Siracusano, N. Van Dijk, E. Payne-johnson, V. Baglio and A. S. Aricò, *Appl. Catal. B, Environ.*, 2015, **164**, 488–495.
10 D. F. Abbott, D. Lebedev, K. Waltar, M. Povia, M. Nachtegaal, E. Fabbri, C. Copéret and T. J. Schmidt, *Chem. Mater.*, 2016, **28**, 6591–6604.
11 C. Felix, B. J. Bladergroen, V. Linkov, B. G. Pollet and S. Pasupathi, *Catalysts*, 2019, **9**, 1–16.
12 M. Faustini, M. Giraud, D. Jones, J. Rozière, M. Dupont, T. R. Porter, S. Nowak, M. Bahri, O. Ersen, C. Sanchez, C. Boissière, C. Tard and J. Peron, *Adv. Energy Mater.*, 2019, **9**, 1–11.
13 S. Siracusano, N. Hodnik, P. Jovanovic, F. Ruiz-Zepeda, M. Šala, V. Baglio and A. S. Aricò, *Nano Energy*, 2017, **40**, 618–632.
14 H. Yu, N. Danilovic, Y. Wang, W. Willis, A. Poozhikunnath, L. Bonville, C. Capuano, K. Ayers and R. Maric, *Appl. Catal. B Environ.*, 2018, **239**, 133–146.
15 C. Van Pham, M. Bühler, J. Knöppel, M. Bierling, D. Seeberger, D. Escalera-López, K. J. J. Mayrhofer, S. Cherevko and S. Thiele, *Appl. Catal. B Environ.*, 2020, **269**, 118762.
16 H. Oh, H. N. Nong, T. Reier, M. Gliech and P. Strasser, *Chem. Sci.*, 2015, **6**, 3321–3328.
17 C. Van Pham, D. Escalera-López, K. Mayrhofer, S. Cherevko and S. Thiele, *Adv. Energy Mater.*, 2021, **11**, 2101998.
18 L. Moriau, M. Smiljanić, A. Lončar and N. Hodnik, *ChemCatChem*, 2022, **14**, e202200586.
19 J. Y. Choi, J. G. Kim, H. J. Lee and C. Pak, *Int. J. Hydrogen Energy*, 2025, **97**, 57–65.
20 C. Baik, J. Cho, J. In, Y. Cho, S. Soon and C. Pak, *J. Power Sources*, 2023, **575**, 233174.
21 T. Reier, Z. Pawolek, S. Cherevko, M. Bruns, T. Jones, D. Teschner, S. Selve, A. Bergmann, H. N. Nong, R. Schlögl, K. J. J. Mayrhofer and P. Strasser, *J. Am. Chem. Soc.*, 2015, **137**, 13031–13040.
22 E. Oakton, D. Lebedev, M. Povia, D. F. Abbott, E. Fabbri, A. Fedorov, M. Nachtegaal, C. Copéret and T. J. Schmidt, *ACS Catal.*, 2017, **7**, 2346–2352.
23 M. Bernt and H. A. Gasteiger, *J. Electrochem. Soc.*, 2016, **163**, F3179–F3189.
24 I. Jiménez-Morales, S. Cavaliere, J. Rozière, M. Dupont and D. Jones, *Sustain. Energy Fuels*, 2019, **3**, 1526–1535.
25 H. P. Tran, H. N. Nong, M. Zlatar, A. Yoon, U. Hejral, M. Rüscher, J. Timoshenko, S. Selve, D. Berger, M. Kroschel, M. Klingenhof, B. Paul, S. Möhle, K. N. Nagi Nasralla, D. Escalera-López, A. Bergmann, S. Cherevko, B. R. Cuenya and P. Strasser, *J. Am. Chem. Soc.*, 2024, **146**, 31444–31455.
26 P. K. Mohanta, C. Glökler, A. O. Arenas and L. Jörissen, *Int. J. Hydrogen Energy*, 2017, **2**, 1–12.
27 I. Jiménez-Morales, S. Cavaliere, D. Jones and J. Rozière, *Phys. Chem. Chem. Phys.*, 2018, **20**, 8765–8772.
28 I. Jiménez-Morales, F. Haidar, S. Cavaliere, D. Jones and J. Rozière, *ACS Catal.*, 2020, **10**, 10399–10411.
29 J. Ma, A. Habrioux, Y. Luo, G. Ramos-Sanchez, L. Calvillo, G. Granozzi, P. B. Balbuena and N. Alonso-Vante, *J. Mater. Chem. A*, 2015, **3**, 11891–11904.
30 H.-S. Oh, H. N. Nong, T. Reier, A. Bergmann, M. Gliech, J. Ferreira de Araújo, E. Willinger, R. Schlögl, D. Teschner and P. Strasser, *J. Am. Chem. Soc.*, 2016, **138**, 12552–12563.
31 Y. Wang, T. Brezesinski, M. Antonietti and B. Smarsly, *ACS Nano*, 2009, **3**, 1373–1378.
32 H. Ohno, S. Nohara, K. Kakinuma, M. Uchida and H. Uchida, *Catalysts*, 2019, **9**, 74.
33 S. Cavaliere, I. Jiménez-Morales, G. Ercolano, I. Savych, D. Jones and J. Rozière, *ChemElectroChem*, 2015, **2**, 1966–1973.
34 S. Cavaliere, S. Subianto, I. Savych, M. Tillard, D. J. Jones and J. Rozière, *J. Phys. Chem. C*, 2013, **117**, 18298–18307.
35 A. T. Marshall and R. G. Haverkamp, *Electrochim. Acta*, 2010, **55**, 1978–1984.
36 D. Böhm, M. Beetz, M. Schuster, K. Peters, A. G. Hufnagel, M. Döblinger, B. Böller, T. Bein and D. Fattakhova-Rohlfing, *Adv. Funct. Mater.*, 2020, **30**, 1906670.
37 T. Reier, D. Teschner, T. Lunkenbein, A. Bergmann, S. Selve, R. Kraehnert, R. Schlögl and P. Strasser, *J. Electrochem. Soc.*, 2014, **161**, F876–F882.
38 M. Möckl, M. F. Ernst, M. Kornherr, F. Allebrod, M. Bernt, J. Byrknes, C. Eickes, C. Gebauer, A. Moskovtseva and H. A. Gasteiger, *J. Electrochem. Soc.*, 2022, **169**, 064505.
39 M. Malinovic, P. Paciok, E. S. Koh, M. Geuß, J. Choi, P. Pfeifer, J. P. Hofmann, D. Göhl, M. Heggen, S. Cherevko and M. Ledendecker, *Adv. Energy Mater.*, 2023, **13**, 2301450.
40 M. Povia, D. F. Abbott, J. Herranz, A. Heinritz, D. Lebedev, B. J. Kim, E. Fabbri, A. Patru, J. Kohlbrecher, R. Schäublin, M. Nachtegaal, C. Copéret and T. J. Schmidt, *Energy Environ. Sci.*, 2019, **12**, 3038–3052.
41 Z. S. H. S. Rajan, T. Binninger, P. J. Kooyman, D. Susac and R. Mohamed, *Catal. Sci. Technol.*, 2020, **10**, 3938–3948.
42 C. Daiane Ferreira Da Silva, F. Claudel, V. Martin, R. Chattot, S. Abbou, K. Kumar, I. Jiménez-Morales, S. Cavaliere, D. Jones, J. Rozière, L. Solà-Hernandez, C. Beauger, M. Faustini, J. Peron, B. Gilles, T. Encinas, L. Piccolo, F. H. Barros De Lima, L. Dubau and F. Maillard, *ACS Catal.*, 2021, **11**, 4107–4116.
43 V. K. Puthiyapura, M. Mamlouk, S. Pasupathi, B. G. Pollet and K. Scott, *J. Power Sources*, 2014, **269**, 451–460.
44 V. Pfeifer, T. E. Jones, J. J. Velasco Vélez, C. Massué, R. Arrigo, D. Teschner, F. Girgsdies, M. Scherzer, M. T. Greiner, J. Allan, M. Hashagen, G. Weinberg, S. Piccinin, M. Hävecker, A. Knop-Gericke and R. Schlögl, *Surf. Interface Anal.*, 2016, **48**, 261–273.
45 F. Karimi, B. A. Peppley and A. Bazylak, *ECS Trans.*, 2015, **69**, 87–98.
46 C. Massué, X. Huang, A. Tarasov, C. Ranjan, S. Cap and R. Schlögl, *ChemSusChem*, 2017, **10**, 1958–1968.

47 V. Pfeifer, T. E. Jones, J. J. Velasco Vélez, R. Arrigo, S. Piccinin, M. Hävecker, A. Knop-Gericke and R. Schlögl, *Chem. Sci.*, 2017, **8**, 2143–2149.

48 H. N. Nong, L. J. Falling, A. Bergmann, M. Klingenhof, H. P. Tran, C. Spöri, R. Mom, J. Timoshenko, G. Zichittella, A. Knop-Gericke, S. Piccinin, J. Pérez-Ramírez, B. R. Cuenya, R. Schlögl, P. Strasser, D. Teschner and T. E. Jones, *Nature*, 2020, **587**, 408–413.

49 Y. S. Huang, S. S. Lin, C. R. Huang, M. C. Lee, T. E. Dann and F. Z. Chien, *Solid State Commun.*, 1989, **70**, 517–522.

50 W. Sun, L. Cao and J. Yang, *J. Mater. Chem. A Mater. Energy Sustain.*, 2016, **4**, 12561–12570.

51 C. Ma, C. Hu, X. Liu, Y. Li, J. Cui, Y. Wu and J. Huang, *ACS Omega*, 2022, **7**, 28985–28993.

52 Z. Pavlovic, C. Ranjan, Q. Gao and M. Van Gastel, *ACS Catal.*, 2016, **6**, 8098–8105.

53 S. Geiger, O. Kasian, B. R. Shrestha, A. M. Mingers, K. J. J. Mayrhofer and S. Cherevko, *J. Electrochem. Soc.*, 2016, **163**, F3132–F3138.

54 S. Cherevko, T. Reier, A. R. Zeradjanin, Z. Pawolek, P. Strasser and K. J. J. Mayrhofer, *Electrochem. commun.*, 2014, **48**, 81–85.

55 G. C. da Silva, N. Perini and E. A. Ticianelli, *Appl. Catal. B Environ.*, 2017, **218**, 287–297.

56 F. Karimi, A. Bazylak and B. A. Peppley, *J. Electrochem. Soc.*, 2017, **164**, F464–F474.

57 J. Cheng, J. Yang, S. Kitano, G. Juhasz, M. Higashi, M. Sadakiyo, K. Kato, S. Yoshioka, T. Sugiyama, M. Yamauchi and N. Nakashima, *ACS Catal.*, 2019, **9**, 6974–6986.

58 J. Ruiz Esquius, D. J. Morgan, I. Spanos, D. G. Hewes, S. J. Freakley and G. J. Hutchings, *ACS Appl. Energy Mater.*, 2020, **3**, 800–809.

59 S. Geiger, O. Kasian, M. Ledendecker, E. Pizzutilo, A. M. Mingers, W. T. Fu, O. Diaz-Morales, Z. Li, T. Oellers, L. Fruchter, A. Ludwig, K. J. J. Mayrhofer, M. T. M. Koper and S. Cherevko, *Nat. Catal.*, 2018, **1**, 508–515.

60 C. Roiron, C. Wang, I. V. Zenyuk and P. Atanassov, *J. Phys. Chem. Lett.*, 2024, **15**, 11217–11223.

61 V. Senthilkumar, P. Vickraman, M. Jayachandran and C. Sanjeeviraja, *J. Mater. Sci. Mater. Electron.*, 2010, **21**, 343–348.

62 Q. Liu, L. Zhang, J. F. Chen and Y. Le, *Mater. Lett.*, 2014, **137**, 339–342.

63 L. P. Yuan, W. J. Jiang, X. L. Liu, Y. H. He, C. He, T. Tang, J. Zhang and J. S. Hu, *ACS Catal.*, 2020, **10**, 13227–13235.

64 S.-C. Sun, H. Jiang, Z.-Y. Chen, Q. Chen, M.-Y. Ma, L. Zhen, B. Song and C.-Y. Xu, *Angew. Chemie Int. Ed.*, 2022, **61**, e202202519.

65 C. Spöri, J. T. H. Kwan, A. Bonakdarpour, D. P. Wilkinson and P. Strasser, *Angew. Chemie - Int. Ed.*, 2017, **56**, 5994–6021.

66 L. Dubau, F. Maillard, M. Chatenet, S. Cavaliere, I. Jiménez-Morales, A. Mosdale and R. Mosdale, *Energies*, 2020, **13**, 403.

67 S. S. Karade, R. Sharma, S. Gyergyek, P. Morgen and S. M. Andersen, *ChemCatChem*, 2023, **15**, e202201470.

68 G. Li, H. Jia, H. Liu, X. Yang and M.-C. Lin, *RSC Adv.*, 2022, **12**, 28929–28936.

69 J. I. Cha, C. Baik, S. W. Lee and C. Pak, *Catal. Today*, 2022, **403**, 19–27.

70 H. Guan, Q. Ke, C. Lv, N. Zeng, C. Hu, S. Wang, X. Ge and J. Cai, *Chem. Lett.*, 2020, **49**, 705–708.

71 S. W. Lee, C. Baik, D. H. Kim and C. Pak, *J. Power Sources*, 2021, **493**, 229689.

72 Y. Liu, M. Zhang, C. Zhang, H. Zhang and H. Wang, *Nanoscale*, 2024, **16**, 9382–9391.

73 J. Islam, S.-K. Kim, M. M. Rahman, P. T. Thien, M.-J. Kim, H.-S. Cho, C. Lee, J. H. Lee and S. Lee, *Mater. Today Energy*, 2023, **32**, 101237.

74 G. H. J. Changsoo Lee, Kihyun Shin, Youngtae Park, Young Hwa Yun, Gisu Doo, H. Y. K. MinJoong Kim, Won-Chul Cho, Chang-Hee Kim, Hyuck Mo Lee and and H.-S. C. Sechan Lee, Graeme Henkelman, *Adv. Funct. Mater.*, 2023, **33**, 2301557.

75 T. Audichon, B. Guenot, S. Baranton, M. Cretin, C. Lamy and C. Coutanceau, *Appl. Catal. B Environ.*, 2017, **200**, 493–502.

76 J. H. Scofield, *J. Electron Spectros. Relat. Phenomena*, 1976, **8**, 129–137.

77 C. C. L. Mccrory, S. Jung, J. C. Peters and T. F. Jaramillo, . J. Am. Chem. Soc. 2013, 135, 45, 16977–16987

78 I. Savych, S. Subianto, Y. Nabil, S. Cavaliere, D. Jones and J. Rozière, *Phys. Chem. Chem. Phys.*, 2015, **17**, 16970–16976.

View Article Online
DOI: 10.1039/D5LF00008D

Data availability

The data supporting this article have been included as part of the Supplementary Information.